Tellus (2005), 57A, 171–182
Printed in UK. All rights reserved

TELLUS

Transparent lateral boundary conditions for baroclinic waves: a study of two elementary systems of equations

By A. McDONALD, *Met Éireann, Glasnevin Hill, Dublin 9, Ireland*

(Manuscript received 30 June 2004; in final form 14 October 2004)

ABSTRACT

Transparent lateral boundary conditions are derived for two linear systems of equations which support baroclinic waves. The first consists of a two-layer model of two superposed immiscible fluids of different densities. The second consists of a multilevel model of the hydrostatic primitive equations in two (x–z) dimensions. A practical demonstration is given of the efficacy of these boundary conditions for both system of equations. First, it is shown that the boundaries are transparent to outgoing waves. Secondly, it is demonstrated that externally imposed incoming waves enter without distortion.

1. Introduction

For the reasons described in the introduction to McDonald (2000), the High-Resolution Limited Area Modelling group (HIRLAM) has initiated a research programme whose objective is to improve its incumbent boundary coupling scheme, that described in Davies (1976, 1983). (For an update on the 'Davies scheme', see Marbaix et al., 2003.) As part of that research programme, this paper addresses the question: can transparent boundary conditions be constructed for baroclinic waves?

In a seminal paper, Engquist and Majda (1977) described a method for dealing with 'open' boundaries, that is, boundaries which are not physical, but rather mathematical constructs forced into the 'initial boundary value problem' by a need to solve it on a computer over regions of space which are not bounded by physical barriers. These regions are usually called 'limited areas' in the meteorological and oceanic communities, possibly because the first models of the atmosphere having open boundaries were two-dimensional. Although their method is very popular with other modelling communities (see Tsynkov, 1998), it has generated only limited interest in the meteorological and oceanic communities. A possible reason is that although it seems to potentially work well for barotropic waves (McDonald, 2002) or sound waves, it seems totally inappropriate for baroclinic waves (see section 3.2 of Durran, 2001).

The purpose of this paper is to argue that there is a way around this obstacle and that it is possible to construct boundary conditions which handle transparently both outgoing, and if desired, simultaneously incoming gravity waves. The latter is important for two reasons. First, it may be useful in the context of oceanic modelling, or at some future date in atmospheric modelling. Secondly, it demonstrates a method of injecting information accurately through the boundary, which is an issue for nested models. The expectation is that a similar approach will also work for more sophisticated models which support the dominant 'slow' waves of the atmosphere or ocean.

Thus, Section 2.1 shows how to build transparent boundary conditions for the simplest possible system of equations that support a baroclinic wave as well as a barotropic wave, that is, that of a model describing two superposed immiscible fluids of different density. The fact that these transparent boundary conditions work well is demonstrated in Section 2.3. Section 3.1 shows how to make transparent boundary conditions for a multilevel model of the two-dimensional linearized hydrostatic primitive equations, which support multiple baroclinic waves. The transparency of these boundary conditions is demonstrated in Section 3.2 by integrating the equations using 10 vertical levels.

2. Two-layer model

The purpose of this section is (1) to derive transparent boundary conditions for the simplest possible system of linear equations which supports a baroclinic wave, and (2) to demonstrate via a practical integration that these boundary conditions work.

The system of equations that describes two superposed immiscible fluids of different density is derived from the conservation of mass and momentum with the Coriolis force set to zero; see chapter 6.2 of Gill (1982), whose notation is used with minor alterations. The equations are

$$\frac{\partial \eta_1}{\partial t} + \bar{u}\frac{\partial \eta_1}{\partial x} + H_1\frac{\partial u_1}{\partial x} + H_2\frac{\partial u_2}{\partial x} = 0, \tag{2.1}$$

e-mail: aidan.mcdonald@met.ie

$$\frac{\partial \eta_2}{\partial t} + \bar{u}\frac{\partial \eta_2}{\partial x} + H_2\frac{\partial u_2}{\partial x} = 0, \tag{2.2}$$

$$\frac{\partial u_1}{\partial t} + \bar{u}\frac{\partial u_1}{\partial x} + g\frac{\partial \eta_1}{\partial x} = 0, \tag{2.3}$$

$$\frac{\partial u_2}{\partial t} + \bar{u}\frac{\partial u_2}{\partial x} + g''\frac{\partial \eta_1}{\partial x} + g'\frac{\partial \eta_2}{\partial x} = 0. \tag{2.4}$$

Here, x and t are the space and time coordinates, $g = 9.81$ is the gravitational acceleration, $\bar{u}$ is a constant advecting velocity, and

$$g'' = g\frac{\rho_1}{\rho_2}; \qquad g' = g\left(1 - \frac{\rho_1}{\rho_2}\right) \tag{2.5}$$

where ρ_1 and ρ_2 are the densities of the upper and lower fluids, respectively. The fields $\eta_1(x, t)$ and $\eta_2(x, t)$ describe the displacement of the fluid surfaces from their resting thicknesses, H_1 and H_2, respectively. Lastly, $u_1(x, t)$ and $u_2(x, t)$ are the horizontal velocity components (see fig. 6.1 of Gill, 1982).

2.1. *Derivation of the boundary conditions*

For a detailed discussion of the following approach to the boundary problem, see chapter 10 of Gustafsson et al. (1995). Taking the Laplace transform of eqs. (2.1)–(2.4) and using property 15 on p. 210 of Doetsch (1971) yields

$$\mathbf{A}\frac{\partial \hat{\mathbf{\Psi}}(x, s)}{\partial x} + s\hat{\mathbf{\Psi}}(x, s) = \mathbf{\Psi}(x, 0_+), \tag{2.6}$$

where $\mathbf{\Psi}$ is the vector $(\eta_1, \eta_2, u_1, u_2)^{\mathrm{t}}$ (superscript 't' denotes transpose) and

$$\hat{\mathbf{\Psi}}(x, s) = \int_0^\infty \mathrm{e}^{-st}\mathbf{\Psi}(x, t)\,\mathrm{d}t. \tag{2.7}$$

Also,

$$\mathbf{A} = \begin{bmatrix} \bar{u} & 0 & H_1 & H_2 \\ 0 & \bar{u} & 0 & H_2 \\ g & 0 & \bar{u} & 0 \\ g'' & g' & 0 & \bar{u} \end{bmatrix}. \tag{2.8}$$

If a matrix $\mathbf{Q}$ can be found which diagonalizes $\mathbf{A}$ then eq. (2.6) can be rearranged into a set of first-order linear differential equations

$$\lambda_k\frac{\partial \hat{W}_k(x, s)}{\partial x} + s\hat{W}_k(x, s) = W_k(x, 0_+). \tag{2.9}$$

Here

$$\mathbf{W} = \mathbf{Q}^{-1}\mathbf{\Psi}, \tag{2.10}$$

and $\mathbf{Q}^{-1}\mathbf{A}\mathbf{Q} = \mathbf{\Lambda}$, where $\mathbf{\Lambda}$ is a diagonal matrix whose non-zero elements are λ_k. The solution of eq. (2.9) is given on p. 21 of Ince (1956):

$$\hat{W}_k(x, s) = \hat{W}_k(x_0, s)\mathrm{e}^{-s(x-x_0)/\lambda_k} + \frac{1}{\lambda_k}\mathrm{e}^{-sx/\lambda_k}\int_{x_0}^{x} W_k(\xi, 0_+)\mathrm{e}^{s\xi/\lambda_k}\,\mathrm{d}\xi. \tag{2.11}$$

The inverse Laplace transform gives the final solution. Consider the first term on the right-hand side of eq. (2.11). Its contribution to the solution is given on p. 209 of Doetsch (1971) as

$$W_k(x, t) = W_k[x_0, t - (x - x_0)/\lambda_k]; \quad t > (x - x_0)/\lambda_k \geq 0, \tag{2.12}$$

$$W_k(x, t) = 0; \qquad t < (x - x_0)/\lambda_k. \tag{2.13}$$

Let the integration region be $0 \leq x \leq L$ and imagine an observer positioned at $x = L/2$. If $\lambda_k > 0$, then at any time after $L/(2\lambda_k)$ the solution is dictated by the boundary value $W_k(0, t)$, as can be seen from substituting $x_0 = 0$ in eq. (2.12). At any time prior to that, the boundary value of W_k does not contribute to the solution. If $\lambda_k < 0$, there is no contribution from the boundary at $x = 0$ because of condition (2.13).

The first implication is that any waves approaching the boundary at $x = 0$ from the interior will be reflected if the imposed boundary fields are such that $W_k(0, t) \neq 0$, for any 'k' such that $\lambda_k > 0$. The second implication is that in a nested environment where the desire is to ensure that only certain types of wave (say mode m with $\lambda_m > 0$) enter the integration area to the exclusion of others, then the imposed boundary fields must be such that $W_m(0, t)$ is finite and that all other $W_k(0, t)$ for which $\lambda_k > 0$ are zero.

For the boundary at $x = L$ the arguments are formally the same. The waves entering the area are now characterized by $\lambda_m < 0$.

The contribution of the initial state to the solution can be deduced by taking the inverse transform of the second term on the right-hand side of eq. (2.11); see property 159 on p. 222 of Doetsch (1971).

The matrix $\mathbf{Q}^{-1}$ can be deduced by finding the eigenvalues and associated left eigenvectors of $\mathbf{A} - \lambda\mathbf{I}$, where $\mathbf{I}$ is a unit matrix. The four eigenvalues, written such that $\lambda_1 > \lambda_2 > \lambda_3 > \lambda_4$, are

$$\begin{aligned} &\lambda_1 = \bar{u} + c_0; \qquad \lambda_2 = \bar{u} + c_1; \\ &\lambda_3 = \bar{u} - c_1; \qquad \lambda_4 = \bar{u} - c_0, \end{aligned} \tag{2.14}$$

where

$$c_0 = \left[\frac{g}{2}(H_1 + H_2)\left\{1 + \left[1 - \frac{4g'H_1H_2}{g(H_1+H_2)^2}\right]^{1/2}\right\}\right]^{1/2}, \tag{2.15}$$

$$c_1 = \left[\frac{g}{2}(H_1 + H_2)\left\{1 - \left[1 - \frac{4g'H_1H_2}{g(H_1+H_2)^2}\right]^{1/2}\right\}\right]^{1/2}. \tag{2.16}$$

The two 'barotropic' waves have velocities $\pm c_0$ and the two 'baroclinic' waves have velocities $\pm c_1$. The associated left eigenvectors up to a normalization give the matrix ($a_0 = 1 - gH_1/c_0^2$ and $a_1 = 1 - gH_1/c_1^2$)

$$\mathbf{Q}^{-1} = \begin{bmatrix} a_1 & -1 & (H_1a_1/c_0) & -(gH_1H_2/c_0c_1^2) \\ a_0 & -1 & (H_1a_0/c_1) & -(gH_1H_2/c_1c_0^2) \\ a_0 & -1 & -(H_1a_0/c_1) & (gH_1H_2/c_1c_0^2) \\ a_1 & -1 & -(H_1a_1/c_0) & (gH_1H_2/c_0c_1^2) \end{bmatrix}, \tag{2.17}$$

whose inverse is

$$\mathbf{Q} = \frac{c_1^2 c_0^2}{2gH_1\left(c_1^2 - c_0^2\right)} \times \begin{bmatrix} 1 & -1 & -1 & 1 \\ a_0 & -a_1 & -a_1 & a_0 \\ (g/c_0) & -(g/c_1) & (g/c_1) & -(g/c_0) \\ (c_0 a_0/H_2) & -(c_1 a_1/H_2) & (c_1 a_1/H_2) & -(c_0 a_0/H_2) \end{bmatrix}. \tag{2.18}$$

Appendix A describes the practical details of translating the imposition of **W** on the boundary into boundary values for the fields η_1 and η_2.

2.2. *Discretization of the equations*

For the spatial discretization, the wind fields are staggered from the height fields, with the height fields at the end points. For the time discretization, the leapfrog scheme is used. Thus, for example, eqs. (2.2) and (2.3) are discretized as

$$\eta_2(i, n+1) = \eta_2(i, n-1) - \frac{\bar{u}\Delta t}{\Delta x} \times [\eta_2(i+1, n) - \eta_2(i-1, n)] - \frac{2H_2\Delta t}{\Delta x} \times \left[u_2\left(i+\frac{1}{2}, n\right) - u_2\left(i-\frac{1}{2}, n\right)\right], \tag{2.19}$$

$$u_1\left(i+\frac{1}{2}, n+1\right) = u_1\left(i+\frac{1}{2}, n-1\right) - \frac{\bar{u}\Delta t}{\Delta x} \times \left[u_1\left(i+\frac{3}{2}, n\right) - u_1\left(i-\frac{1}{2}, n\right)\right] - \frac{2g\Delta t}{\Delta x}\left[\eta_1(i+1, n) - \eta_1(i, n)\right], \tag{2.20}$$

where $x = i\Delta x$, $L = I\Delta x$ and $t = n\Delta t$. Equations (2.1) and (2.4) are discretized in exactly the same way. The boundary fields, $\eta_1(0, n+1)$, $\eta_2(0, n+1)$, $\eta_1(I, n+1)$ and $\eta_2(I, n+1)$, must be supplied. How to do this is discussed in Appendix A. A Robert (1966) filter is used to control the computational mode. Equation (2.19) is valid from $i = 1$ to $i = I - 1$. Equation (2.20) is valid from $i = 0$ (where a right derivative is used for the advection term) to $i = I - 1$ (where a left derivative is used for the advection term).

2.3. *Testing the boundary conditions*

In this section a practical demonstration is given of the boundary conditions derived in Section 2.1. First, it is shown that the boundaries are transparent to outgoing waves: there is no reflection. Secondly, it is shown that they are transparent to externally imposed incoming waves: they enter without distortion.

The parameters are $\Delta x = 10$ km, $\Delta t = 9.0$ s, $g' = 4.09$, $g'' = 5.72$, $H_1 = 5000$ m and $H_2 = 5000$ m. These result in $c_0 = 294.1$ m s^{-1} and $c_1 = 107.6$ m s^{-1}. The values of g' and g'' result from using the International Civil Aviation Office densities at 7500 m ($\rho_1 = 0.56$ kg m^{-3}) and 2500 m ($\rho_2 = 0.96$ kg m^{-3}); see, for example, table A14 of Met.O.1012 (1993). For the tests described in this section, $\bar{u} = 0$. The complications caused by non-zero $\bar{u}$ are probed in Section 3.2.

Two sets of integrations were performed with the same Δx and Δt: one with $L = 1000$ km, $I = 101$, and a second 'host integration' with $L^{\mathrm{h}} = 10\,000$ km, $I^{\mathrm{h}} = 1001$. The latter integration, whose boundaries are so far removed that no waves can travel to them and back to the boundary of the guest area during the length of the integration, is used as the 'correct integration' with which the test integrations will be compared. It is also used to furnish the boundary fields to drive the integration in 'test 2' below.

Test 1: are the boundaries transparent for out-going waves?. The initial state consisted of a bell-shape distortion of the two surfaces centred at $L/2$ (see Fig. 1). The bell can be written as

$$B(x, x_{\mathrm{s}}, \Gamma_{\mathrm{s}}) = \exp\left\{-\left[\frac{(x - x_{\mathrm{s}})}{\Gamma_{\mathrm{s}}}\right]^2\right\}, \tag{2.21}$$

where x_{s} is the starting position and Γ_{s} is the half-width of the bell. Using this generic formula, the initial state is given by

$$\eta_1(x, 0) = AB(x, L/2, L/20), \qquad \eta_2(x, 0) = -\eta_1(x, 0)$$
$$u_1(x, 0) = 0, \qquad u_2(x, 0) = 0, \tag{2.22}$$

where $A = 10$ m. For the 'host integration' $L^{\mathrm{h}}/2$ replaces $L/2$ in eq. (2.22)

This initial state contains a combination of all four waves, the 'mode 0' waves having amplitude $A(2 - gH_1/c_1^2)$ and the 'mode 1' waves having amplitude $A(2 - gH_1/c_0^2)$, as can be seen by substituting eq. (2.22) into eq. (2.10). Once the integration starts, the 'mode 0' waves travel in the $\pm$ direction with a velocity $\pm c_0$, and the 'mode 1' waves travel in the $\pm$ direction with a velocity $\pm c_1$. Thus, for instance, after 23.25 min the apexes of the 'mode

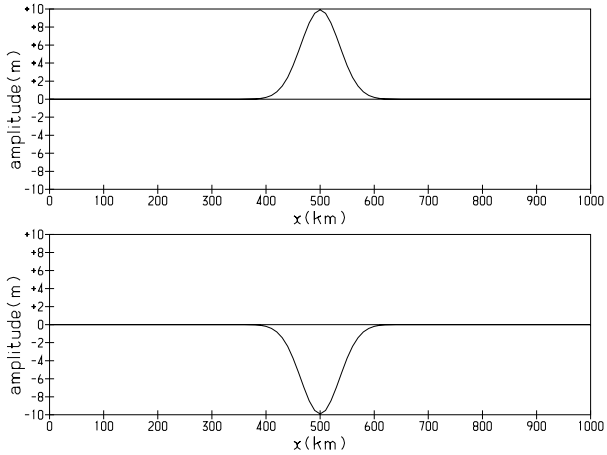

Fig 1. The fields η_1 (top) and η_2 (bottom) at the initial time.

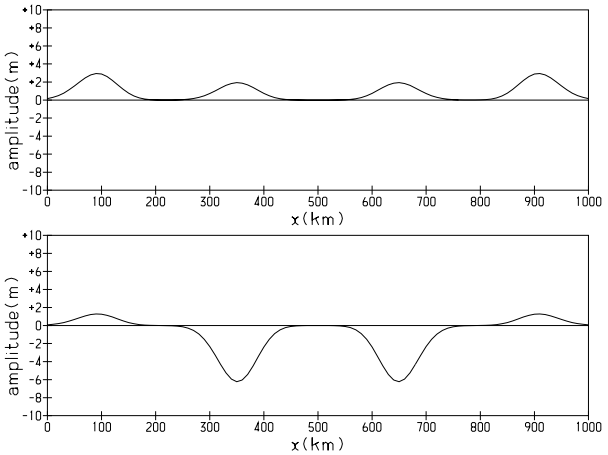

Fig 2. The fields η_1 (top) and η_2 (bottom) after 23.25 min.

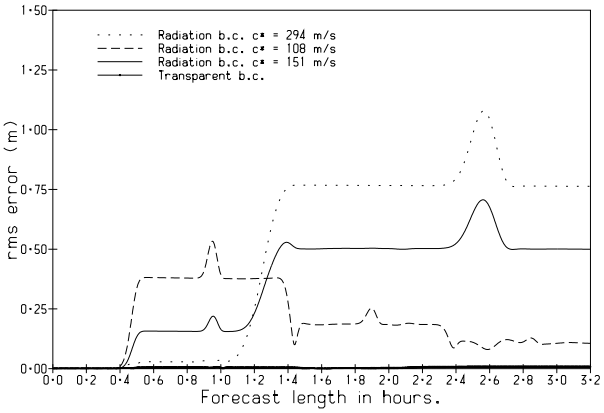

Fig 3. The combined rms error of η_1 and η_2 using radiation boundary conditions with three different values of c^* and transparent boundary conditions.

0' ('mode 1') bell-shapes will have moved a distance ± 410 km (± 150 km), as is demonstrated in Fig. 2.

The eigenvalues λ_1 and λ_2 are greater than zero ($l = 2$ in Appendix A). Thus, imposing W_1 and W_2 ensures the integration proceeds correctly at $x = 0$. The eigenvalues λ_3 and λ_4 are less than zero. Thus, imposing W_3 and W_4 ensures the integration proceeds correctly at $x = L$.

To see whether these waves will exit without reflection as the integration proceeds, the boundary fields given by eq. (A8) with $\Psi_m = \eta_m$, $m = 1, 2$ are used. These are arrived at by replacing eq. (A1) with

$$W_1\left(\frac{1}{2}, n+1\right) = W_2\left(\frac{1}{2}, n+1\right) = 0$$

and by replacing eq. (A3) with

$$W_3\left[\left(I - \frac{1}{2}\right), n+1\right] = W_4\left[\left(I - \frac{1}{2}\right), n+1\right] = 0.$$

The fact that the boundary conditions perform well is demonstrated in Fig. 3, which shows the rms error for η_1 and η_2 combined. The rms error at the end of the integration is 0.008 m.

To give an indication of how successful these boundary conditions are, Fig. 3 also shows the rms errors for the 'radiation boundary conditions' (see, for example, Durran et al., 1993), implemented using the upstream scheme, which, for instance at $x = L$ looks like

$$\eta(I, n+1) = \left(1 - c^*\frac{\Delta t}{\Delta x}\right)\eta(I, n) + c^*\frac{\Delta t}{\Delta x}\eta(I-1, n) \tag{2.23}$$

for both η_1 and η_2. Three different values of c^* were tested: c_0, c_1 and $(c_0 + c_1)/2$. As can be seen from Fig. 3, using $c^* = c_1$ worked well for the 'mode 0' waves, but not so well for the 'mode 1' waves, and vice versa. [It may, of course, be possible to 'tune' c^* to obtain smaller errors, as is discussed in Durran et al. (1993). It is probably worth remarking that an additional attractive feature of the boundary conditions being proposed in this paper is that there are no 'tuning parameters'.] In Fig. 3 the maxima at 0.94 h and 1.88 h are due to the 'mode 0' waves reflected from the boundaries overlapping as they cross travelling in opposite directions to generate a large amplitude which the rms measure of error exaggerates. Similarly, the bump at 2.58 h is caused by the reflection of the 'mode 1' waves.

Test 2: are the boundaries transparent for incoming waves?. The purpose of this test is to show that waves from an external source can be injected accurately into the integration area. Thus, it is assumed that the following is known from data or from a larger scale model: a (1+) mode initially positioned outside the area at $x = -L/2$ crosses the boundary at $x = 0$ during the integration and is positioned at $x = +L/4$ at the end of the integration. Can the boundary conditions described in Appendix A accurately model this scenario? [Physically, this is an unlikely scenario for a meteorological integration, where gravity waves are regarded mostly as 'noise', but not so outlandish for an oceanic integration (see, for example, p. 126 of Gill, 1982). Nevertheless, the same parameters are used as in test 1, since the aim is simply to establish the principle that accurate nesting is achievable for this simple system of equations.]

To generate the boundaries for this integration, a forecast was run on the host area with the initial state consisting of a mode (1+) bell-shape centred at $x^{\mathrm{h}} = L^{\mathrm{h}}/2 - L$. This was integrated for 116 min, at which time the mode (1+) bell-shape was centred at $x^{\mathrm{h}} = L^{\mathrm{h}}/2 + L/4$. The field $\mathbf{\Psi}^{\mathrm{h}}(x^{\mathrm{h}} = L^{\mathrm{h}}/2 - L/2 + \Delta x/2)$ was computed at every time-step and written to a file. During the nested forecast, this field was read in at each time-step and used to generate the externally supplied boundary field W_2 (1/2, $n + 1$) in eq. (A1). To make the integration more challenging, the same initial state was used as in test 1. Thus, $W_1(1/2, n + 1) = 0$ replaces eq. (A1) and $[W_i[(I - 1/2), n + 1] = 0$, $i = 3, 4$ replaces eq. (A3). Now, four bells will exit and one will enter during the integration. Also, after 77 min of integration at

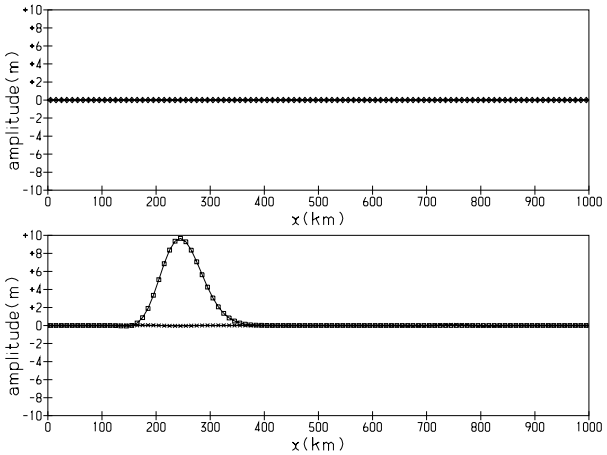

Fig 4. The fields W_1 (top, diamonds), W_4 (top, plus symbols), W_2 (bottom, squares) and W_3 (bottom, times symbols) after 116 min.

$x = 0$ there will be a (1+) mode entering and a (1−) mode exiting simultaneously.

Figure 4 plots the values of the four W fields after 116 min. The (1+) mode has the correct amplitude and is in the correct position (the apex should be at $x = 250$ km). All the other modes have invisible amplitudes, indicating that they have exited without reflection. The rms error for the height field confirms the picture painted by Fig. 4. It was less than 0.03 m throughout the run.

It is fair to conclude from the successful outcome of tests 1 and 2 that the transparent boundary conditions derived in Section 2.1 are amenable to discretization. This inspires the confidence to take the next step, that is, to do the same for a more realistic multilevel model.

3. Multilevel model

In this section, transparent boundary conditions are derived for a system of equations, the two-dimensional linearized hydrostatic primitive equations, which supports multiple baroclinic waves. Also, a practical demonstration is given of their transparency.

3.1. The equations

The linearized inviscid hydrostatic primitive equations in x–z coordinates can be written as follows (see Gill, 1982 for a description of the approximations involved in arriving at this linearization, and, in particular, see section 6.11 of his book for a discussion of the analytical solutions):

$$\rho_0(z)\frac{\mathrm{d}u'(x,z,t)}{\mathrm{d}t} + \frac{\partial p'(x,z,t)}{\partial x} = 0, \tag{3.1}$$

$$\frac{\mathrm{d}\rho'(x,z,t)}{\mathrm{d}t} + \frac{\mathrm{d}\rho_0(z)}{\mathrm{d}z}w'(x,z,t) = 0, \tag{3.2}$$

$$\frac{\partial p'(x,z,t)}{\partial z} + g\rho'(x,z,t) = 0, \tag{3.3}$$

$$\frac{\partial u'(x,z,t)}{\partial x} + \frac{\partial w'(x,z,t)}{\partial z} = 0. \tag{3.4}$$

In these equations, the pressure p', the density ρ' and the x- and z-components of the winds u' and w' are small deviations from an isothermal atmosphere, whose fields are designated by the subscript zero and whose density is $\rho_0(z)$.

There are lateral boundary complications caused by non-zero horizontal velocities. Defining

$$\frac{\mathrm{d}}{\mathrm{d}t} = \frac{\partial}{\partial t} + u_0\frac{\partial}{\partial x}, \tag{3.5}$$

where u_0 is a constant, allows us to discuss them below.

To reduce typographical clutter later in this section, we define $p = p'$, $\rho = \rho'$, $u = \rho_0 u'$ and $w = \rho_0 w'$. Then eqs. (3.1)–(3.4) become

$$\frac{\mathrm{d}u(x,z,t)}{\mathrm{d}t} + \frac{\partial p(x,z,t)}{\partial x} = 0, \tag{3.6}$$

$$\frac{\mathrm{d}\rho(x,z,t)}{\mathrm{d}t} - \frac{N^2(z)}{g}w(x,z,t) = 0, \tag{3.7}$$

$$\frac{\partial p(x,z,t)}{\partial z} + g\rho(x,z,t) = 0. \tag{3.8}$$

$$\frac{\partial u(x,z,t)}{\partial x} + \frac{\partial w(x,z,t)}{\partial z} + \frac{N^2(z)}{g}w(x,z,t) = 0, \tag{3.9}$$

where the Brunt–Väisälä frequency, N^2, is defined in terms of the density of the isothermal atmosphere as

$$N^2(z) = -\frac{g}{\rho_0(z)}\frac{\mathrm{d}\rho_0(z)}{\mathrm{d}z}. \tag{3.10}$$

Discretizing in the vertical and defining the ρ and u fields on the 'full' levels, and the p and w fields on the 'half' levels, gives rise to the following set of equations:

$$\frac{\mathrm{d}u_m(x,t)}{\mathrm{d}t} + \frac{\partial p_m(x,t)}{\partial x} = 0, \tag{3.11}$$

$$\frac{\mathrm{d}\rho_m(x,t)}{\mathrm{d}t} - \frac{N_m^2}{g}w_m(x,t) = 0, \tag{3.12}$$

$$\frac{p_{m+(1/2)}(x,t) - p_{m-(1/2)}(x,t)}{\Delta z_m} + g\rho_m(x,t) = 0. \tag{3.13}$$

$$\frac{\partial u_m(x,t)}{\partial x} + \frac{w_{m+(1/2)}(x,t) - w_{m-(1/2)}(x,t)}{\Delta z_m} + \frac{N_m^2}{g}w_m(x,t) = 0. \tag{3.14}$$

It is important to emphasize that p_m and w_m are defined by the average of the two adjacent half-levels:

$$p_m \equiv \frac{1}{2}\left[p_{m+(1/2)}(x,t) + p_{m-(1/2)}(x,t)\right];$$
$$w_m \equiv \frac{1}{2}\left[w_{m+(1/2)}(x,t) + w_{m-(1/2)}(x,t)\right]. \tag{3.15}$$

Also,

$$\Delta z_m \equiv z_{m+(1/2)} - z_{m-(1/2)}. \tag{3.16}$$

Finally, it is necessary to define boundary conditions at the top of the atmosphere, $z_{1/2}$, and at the bottom of the atmosphere, $z_{M+(1/2)}$, where M is the number of full levels. In the absence of orography, the physical boundary condition at the bottom is

$$w_{M+(1/2)} = 0. \tag{3.17}$$

At the top of the atmosphere, the boundary condition $w_{1/2} = 0$ kills the external mode (see Kalnay, 2003, p. 46). Consequently, a material boundary is used at the top in order to retain this mode:

$$\frac{\mathrm{d}p_{1/2}(x,t)}{\mathrm{d}t} - g w_{1/2}(x,t) = 0. \tag{3.18}$$

Defining $a_m^{\pm} = [1 \pm \Delta z_m N_m^2/(2g)]$, multiplying eq. (3.14) by Δz_m, and summing over m yields a recursive relation for $w_{m-(1/2)}$:

$$w_{m-(1/2)}(x,t) = \frac{1}{a_m^-}\left[\Delta z_m \frac{\partial u_m(x,t)}{\partial x} + a_m^+ w_{m+(1/2)}(x,t)\right]. \tag{3.19}$$

This, combined with eq. (3.17), facilitates the replacement of eq. (3.14) with the following two equations:

$$w_m(x,t) = -\frac{g}{N_m^2}\sum_{j=1}^{M} \tau_{m,j}\frac{\partial u_j(x,t)}{\partial x}, \tag{3.20}$$

$$w_{1/2}(x,t) = -\frac{1}{g}\sum_{j=1}^{M} \nu_j \frac{\partial u_j(x,t)}{\partial x}. \tag{3.21}$$

The matrix $\boldsymbol{\tau}$ and the transposed vector $\boldsymbol{\nu}$ are functions of Δz, N^2 and g only. Although algebraically complicated, they are rather easy to generate in a computer program because of their recursiveness. The factors in front of eqs. (3.20) and (3.21) are included to make eqs. (3.27) and (3.28) look more elegant.

Multiplying eq. (3.13) by Δz_m and summing from the bottom up results in

$$p_m(x,t) = p_{M+(1/2)} + g\left(\frac{\Delta z_m}{2}\rho_m + \sum_{j=m+1}^{M}\Delta z_j \rho_j\right), \tag{3.22}$$

and acts as a reminder that the pressures at the top and bottom of the atmosphere are not independent quantities:

$$p_{1/2} = p_{M+(1/2)} + g\sum_{j=1}^{M}\Delta z_j \rho_j. \tag{3.23}$$

Introducing the vector notation $v = (v_1, v_2, \ldots, v_M)^{\mathrm{t}}$ and defining of $\boldsymbol{\gamma}$ and $\boldsymbol{\eta}$ via

$$(\boldsymbol{\gamma v})_m = g\left(\frac{\Delta z_m}{2}v_m + \sum_{j=m+1}^{M}\Delta z_j v_j\right), \tag{3.24}$$

$$\boldsymbol{\eta . v} = -g\sum_{j=1}^{M}\Delta z_j v_j, \tag{3.25}$$

the equations to be solved become eqs. (3.26)–(3.29):

$$\frac{\mathrm{d}\mathbf{u}(x,t)}{\mathrm{d}t} + \frac{\partial \mathbf{p}(x,t)}{\partial x} = 0, \tag{3.26}$$

$$\frac{\mathrm{d}\boldsymbol{\rho}(x,t)}{\mathrm{d}t} + \boldsymbol{\tau}\frac{\partial \mathbf{u}(x,t)}{\partial x} = 0, \tag{3.27}$$

$$\frac{\mathrm{d}p_{1/2}(x,t)}{\mathrm{d}t} + \boldsymbol{\nu .}\frac{\partial \mathbf{u}(x,t)}{\partial x} = 0, \tag{3.28}$$

$$\mathbf{p}(x,t) = p_{1/2} + \boldsymbol{\eta . \rho}(x,t) + \boldsymbol{\gamma \rho}(x,t). \tag{3.29}$$

To arrive at a solution, differentiate eq. (3.29) with respect to t and substitute eqs. (3.27) and (3.28) in the resulting equation to obtain

$$\frac{\mathrm{d}\mathbf{p}}{\mathrm{d}t} + \mathbf{M}\frac{\partial \mathbf{u}(x,t)}{\partial x}, \tag{3.30}$$

where

$$\mathbf{M} = \boldsymbol{\nu .} + \boldsymbol{\eta\tau .} + \boldsymbol{\gamma\tau}. \tag{3.31}$$

Here, the 'dot' conveys the fact that, if v is any vector, then both $\boldsymbol{\nu}\,.\,\boldsymbol{v}$ and $\boldsymbol{\eta\tau}\,.\,\boldsymbol{v}$ are scalar quantities whereas $\boldsymbol{\gamma\tau v}$ is a vector. Assume there exists a matrix $\mathbf{E}$ which diagonalizes $\mathbf{M}$

$$\mathbf{E}^{-1}\mathbf{M}\mathbf{E} = \mathbf{C^2}, \tag{3.32}$$

where the diagonal matrix has been written as $\mathbf{C^2}$ for later convenience. The diagonal elements are defined as $C_{m,m} = c_m$. Using eq. (3.32), eqs. (3.26) and (3.30) can be rewritten as

$$\frac{\mathrm{d}(\mathbf{E^{-1}u})_m}{\mathrm{d}t} + \frac{\partial(\mathbf{E^{-1}p})_m}{\partial x} = 0, \tag{3.33}$$

$$\frac{\mathrm{d}(\mathbf{E^{-1}p})_m}{\mathrm{d}t} + c_m^2\frac{\partial(\mathbf{E^{-1}u})_m}{\partial x} = 0. \tag{3.34}$$

Defining

$$W_m^{\pm} = \pm(\mathbf{E^{-1}u})_m + \frac{1}{c_m}(\mathbf{E^{-1}p})_m \tag{3.35}$$

enables the transformation of eqs. (3.33)–(3.34) into a form

$$\frac{\partial W_m^{\pm}}{\partial t} + (u_0 \pm c_m)\frac{\partial W_m^{\pm}}{\partial x} = 0, \tag{3.36}$$

such that its Laplace transform is given by eq. (2.9).

Thus, at the western boundary for instance, if any of the fields $W_m^{\pm}(x,t)$ such that $u_0 \pm c_m > 0$ are non-zero at any time t, then $L/[2(u_0 \pm c_m)]$ seconds later this value of the field will have been transported to the centre of the integration area. Since

in a meteorological context this is usually undesirable, it is incumbent to make sure that the boundary conditions are imposed in such a way that $W_m^{\pm}(x, t) = 0$ for these values of m. It is possible to envisage scenarios, particularly in an oceanographic context, where it was known that particular modes were entering the integration area. Then, the particular $W_m^{\pm}(x, t)$ associated with these modes must be assigned their known values and the others associated with incoming waves put to zero.

To put the solutions in the form of eq. (2.10), first, order the eigenvalues such that $c_1 > c_2 > \ldots > c_M > -c_M > -c_{M-1} > \ldots - c_1$; secondly, write $\mathbf{\Psi} = (\mathbf{p}, \mathbf{u})$; and finally, use eq. (3.35) to obtain the characteristic looking combinations for $m = 1, M$

$$W_m = W_m^+ = (\boldsymbol{C}^{-1}\mathbf{E}^{-1}\mathbf{p} + \mathbf{E}^{-1}\mathbf{u})_m, \tag{3.37}$$

$$W_{2M+1-m} = W_m^- = (\boldsymbol{C}^{-1}\mathbf{E}^{-1}\mathbf{p} - \mathbf{E}^{-1}\mathbf{u})_m, \tag{3.38}$$

from which the matrix $\mathbf{Q^{-1}}$ can be built. The matrix $\mathbf{Q}$ can be built using eqs. (3.37) and (3.38):

$$(\mathbf{QW})_{m,j} = p_m = \frac{1}{2}\sum_{j=1}^{M}(\mathbf{EC})_{m,j}(W_j + W_{2M+1-j}); \quad m = 1, M \tag{3.39}$$

$$(\mathbf{QW})_{M+m,j} = u_m = \frac{1}{2}\sum_{j=1}^{M} E_{m,j}(W_j - W_{2M+1-j}); \quad m = 1, M. \tag{3.40}$$

For instance, W_1 is the field associated with $\bar{u} + c_1$ and W_{2M} is the field associated with $\bar{u} - c_1$.

3.2. *Testing the boundary conditions*

In this section, a practical demonstration is given of the transparency of the boundary conditions derived in Appendix A. First, it is shown that the boundaries are transparent to outgoing waves: there is almost no reflection. Secondly, it is shown that they are transparent to an externally imposed incoming wave: it enters almost without distortion.

Equations (3.11)–(3.14) are solved using the leapfrog scheme to discretize in time. For the horizontal spatial discretization, the wind fields are staggered from the density and pressure fields, with the latter two fields at the end points:

$$u_m\left(i+\frac{1}{2}, n+1\right) = u_m\left(i+\frac{1}{2}, n-1\right) - \frac{\bar{u}\Delta t}{\Delta x} \times \left[u_m\left(i+\frac{3}{2}, n\right) - u_m\left(i-\frac{1}{2}, n\right)\right] - \frac{2\Delta t}{\Delta x}\left[p_m(i+1, n) - p_m(i, n)\right], \tag{3.41}$$

$$\rho_m(i, n+1) = \rho_m(i, n-1) - \frac{\bar{u}\Delta t}{\Delta x} \times [\rho_m(i+1, n) - \rho_m(i-1, n)] - \frac{2\Delta t}{\Delta x} \times \left[[\boldsymbol{\tau}\mathbf{u}]_m\left(i+\frac{1}{2}, n\right) - [\boldsymbol{\tau}\mathbf{u}]_m\left(i-\frac{1}{2}, n\right)\right], \tag{3.42}$$

$$p_{1/2}(i, n+1) = p_{1/2}(i, n-1) - \frac{\bar{u}\Delta t}{\Delta x} \times \left[p_{1/2}(i+1, n) - p_{1/2}(i-1, n)\right] - \frac{2\Delta t}{\Delta x} \times \left[\boldsymbol{\nu}.\mathbf{u}\left(i+\frac{1}{2}, n\right) - \boldsymbol{\nu}.\mathbf{u}\left(i-\frac{1}{2}, n\right)\right], \tag{3.43}$$

$$p_m(i, n) = p_{1/2}(i, n) + \boldsymbol{\eta}.\boldsymbol{\rho}(i, n) + \boldsymbol{\gamma}\boldsymbol{\rho}(i, n). \tag{3.44}$$

The boundary fields, $\rho_m(0, n+1)$, $p_{1/2}(0, n+1)$, $\rho_m(I, n+1)$ and $p_{1/2}(I, n+1)$, must be supplied. How to do this is discussed in Appendix A. A Robert (1966) filter is used to control the computational mode. Equation (3.41) is valid from $i = 0$ (where a right derivative is used for the advection term) to $= I - 1$ (where a left derivative is used for the advection term). Equations (3.42) and (3.43) are valid from $i = 1$ to $i = I - 1$.

For an isothermal atmosphere, $N^2 = g^2/(RT_0)$, with T_0 a constant. The value $T_0 = 250$ K was used; $R = 287.04$ J kg^{-1} K^{-1}. For the discretization, $\Delta x = 10$ km, $\Delta t = 9.0$ s, $z_{1/2} = 10$ km; $M = 10$ and the levels are equally spaced; thus $\Delta z_m = -1$ km. These result in $c_1 = 281.6$, $c_2 = 101.2$, $c_3 = 54.2$, $c_4 = 35.3$, $c_5 = 24.9$, $c_6 = 18.2$, $c_7 = 13.2$, $c_8 = 9.3$, $c_9 = 5.9$, $c_{10} = 2.9$, all of these having units of m s^{-1}.

The advecting velocity was chosen to be $\bar{u} = 25$ m s^{-1}. This furnishes a more severe test of the boundary strategy because at $x = 0$, modes 1–16 will be entering and modes 17–20 exiting the area and at $x = L$, modes 17–20 will be entering and modes 1–16 exiting the area.

Test 1: are the boundaries transparent for outgoing waves?. The initial state contains four modes: $W_3(\bar{u} + c_3 = 79.2)$, $W^7(\bar{u} + c_7 = 38.2)$, $W_{19}(\bar{u} - c_2 = -76.2)$ and $W_{20}(\bar{u} - c_1 = -256.6)$. In the x-direction, the fields are bell-shaped and centred at $L/2$. We define

$$\breve{p}_l^m = Q_{l,m}, \qquad \breve{u}_l^m = Q_{l+M,m} \qquad l = 1, M, \qquad m = 1, 2M, \tag{3.45}$$

where $\mathbf{Q}$ is defined via eqs. (3.39) and (3.40) and

$$\breve{p}_l^m = \sum_{j=1}^{M}[\boldsymbol{\tau}\mathbf{E}\boldsymbol{C}^{-2}\mathbf{E}^{-1}]_{l,j}\breve{p}_j^m, \tag{3.46}$$

$$\breve{p}_{1/2}^m = \sum_{j=1}^{M}[\boldsymbol{\nu}\mathbf{E}\boldsymbol{C}^{-2}\mathbf{E}^{-1}]_j\breve{p}_j^m. \tag{3.47}$$

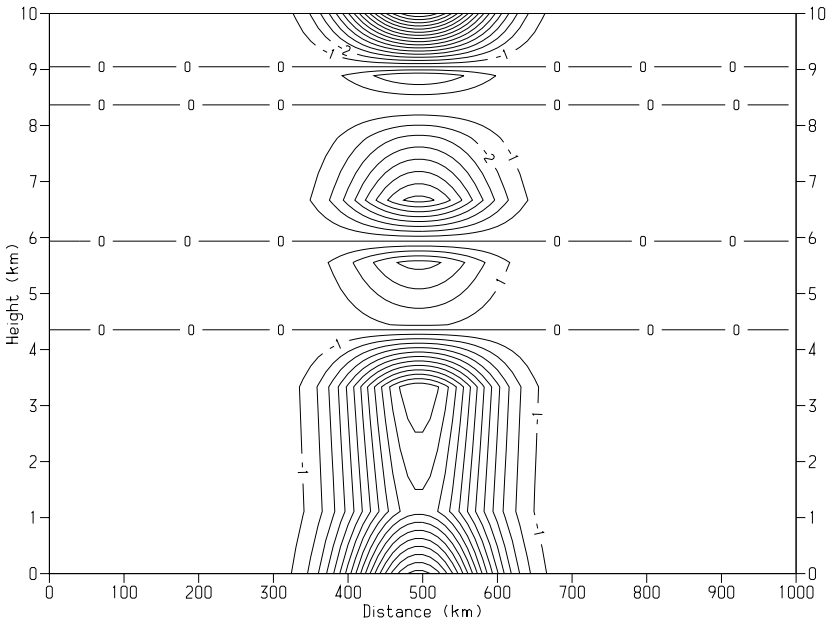

Fig 5. The wind anomaly u' at the initial time.

The initial state, for which the u' field is displayed in Fig. 5, is given by

$$\begin{aligned} u_l(x,0) &= \left(A_3\breve{u}_l^3 + A_7\breve{u}_l^7 + A_{19}\breve{u}_l^{19} + A_{20}\breve{u}_l^{20}\right) \\ &\quad \times B(x, L/2, L/10), \\ \rho_l(x,0) &= \left(A_3\breve{\rho}_l^3 + A_7\breve{\rho}_l^7 + A_{19}\breve{\rho}_l^{19} + A_{20}\breve{\rho}_l^{20}\right) \\ &\quad \times B(x, L/2, L/10), \\ p_l(x,0) &= \left(A_3\breve{p}_l^3 + A_7\breve{p}_l^7 + A_{19}\breve{p}_l^{19} + A_{20}\breve{p}_l^{20}\right) \\ &\quad \times B(x, L/2, L/10), \\ p_{1/2}(x,0) &= \left(A_3\breve{p}_{1/2}^3 + A_7\breve{p}_{1/2}^7 + A_{19}\breve{p}_{1/2}^{19} + A_{20}\breve{p}_{1/2}^{20}\right) \\ &\quad \times B(x, L/2, L/10), \end{aligned} \tag{3.48}$$

where the amplitudes A_m were chosen such that the maximum value of $|u'_m(x,0)|$ equals 10 m s^{-1}. (Recall that $\mathbf{u}' = \mathbf{u}/\rho_0$.)

The sole reason for choosing this initial state is to generate reasonably clutter-free and interpretable figures. (Modes 6–15 move at similar speeds and they contain between five and nine nodes. Including large numbers of these modes makes for hopelessly cluttered figures.)

Since, for the purpose of this test, all incoming waves are being regarded as undesirable 'noise', it is necessary to ensure none of them is excited by the boundary treatment. This is accomplished as follows. Modes 1–16 are travelling in the $+x$-direction. Thus, as was argued in Section 2.1, imposing W_1–W_{16} at the western boundary ensures the integration proceeds correctly there. To ensure none of these modes enters the area, replace eq. (A1) with $W_m = 0$; $m = 1, 16$, and build the boundary fields as described there (with $l = 16$). Also, modes 17–20 are travelling in the $-x$-direction, and imposing W_{17}–W_{20} at the eastern boundary ensures the integration proceeds correctly there. To ensure none of them enters the area, replace eq. (A3) with $W_j = 0$; $j = 17, 20$ and follow the derivation there.

After 32.4 min of integration time had elapsed, the apexes of the mode 3, 7, 19 and 20 waves had travelled distances of 154, 74, −148 and −499 km, respectively, as can be seen in Fig. 6, which shows the u' field. The apex of mode 20, which has no nodes, has reached the western boundary; notice the absence of reflections. Mode 19, which has one node, is easily recognizable; its apex is at $x = 352$ km, as it should be. Modes 3 and 7 are still intertwined.

After 108 min of integration time had elapsed, the apexes of the mode 3, 7, 19 and 20 waves had travelled distances of 514, 248, −494 and −1663 km, respectively. Consider Fig. 7, which displays the u' field at that time. Mode 20 has successfully exited the area with no visible reflections. The apex of mode 19, which has one node, has just reached the western boundary; notice the absence of reflections. The apex of mode 3, which has two nodes, has just passed the eastern boundary; notice the absence of reflections. Mode 7, which has six nodes, is now easily recognizable; its apex is at x =747 km, as it should be.

After 237.6 min of integration time had elapsed, the mode 3, 7, 19 and 20 waves had travelled distances of 1130, 545, −1086 and −3658 km, respectively. Fig. 8 displays the u' field at that time. Modes 20, 19 and 3 have successfully exited the area with no visible reflections. The apex of mode 7, which has six nodes, has already passed through the eastern boundary; notice that if there were any reflections their maximum value is less than 0.5 m s^{-1} because the contouring package rounds upward.

A discussion of the quantitative size of the errors is given after test 2 has been described in order to avoid repetition.

Test 2: are the boundaries transparent for incoming waves? The purpose of this experiment is to show that waves from an

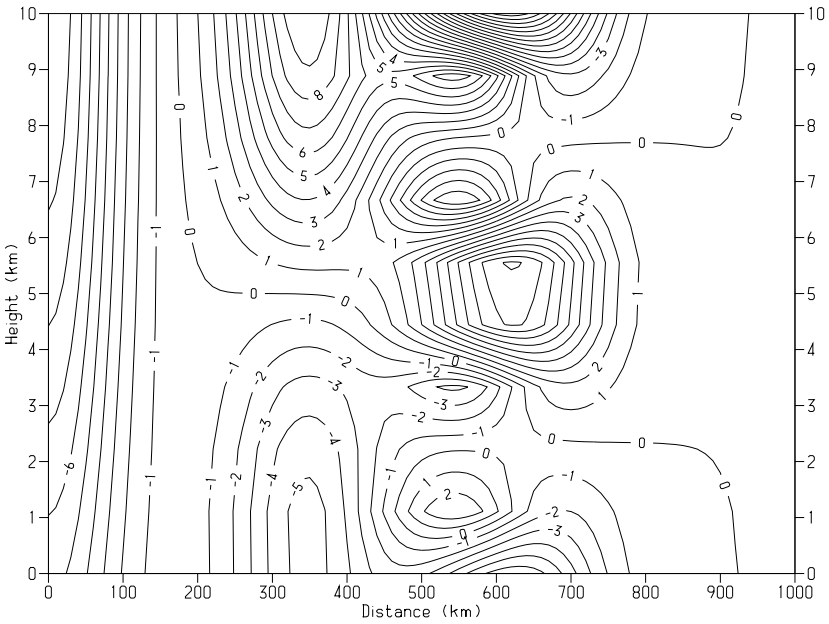

Fig 6. The wind anomaly u' after 32.4 min.

external source can be injected accurately into the integration area. Thus, it is assumed that the following is known from data or from a larger-scale model: a 'mode 4 bell' initially positioned outside the area at $x = -L/2$ crosses the boundary at $x = 0$ during the integration. Can the boundary conditions described in Appendix A accurately model this scenario?

Two sets of integrations were performed: one with $L =$ 1000 km, $I = 101$, and a second 'host integration' with $L^{\mathrm{h}} = 10\,000$ km, $I^{\mathrm{h}} = 1001$. The latter integration furnished the boundary fields describing an incoming mode.

To make the integration more challenging, the same guest area initial state was used as in test 1. Thus, there were five waves exiting and one entering the guest area during the integration. To generate its boundaries, a forecast was run on the host area with the initial state consisting of the same four modes as in test 1 centred at $x^{\mathrm{h}} = L^{\mathrm{h}}/2$ plus a mode 4 bell-shape centred at $x^{\mathrm{h}} = L^{\mathrm{h}}/2 - L$. This was integrated for 9 h, at which time the mode 4 bell-shape was centred at $x^{\mathrm{h}} = L^{\mathrm{h}}/2 + 1954$ km. The field $\mathbf{\Psi}^{\mathrm{h}}(x^{\mathrm{h}} = L^{\mathrm{h}}/2 - L/2 + \Delta x/2)$ was computed at every time-step and written to a file. During the guest forecast, this field was

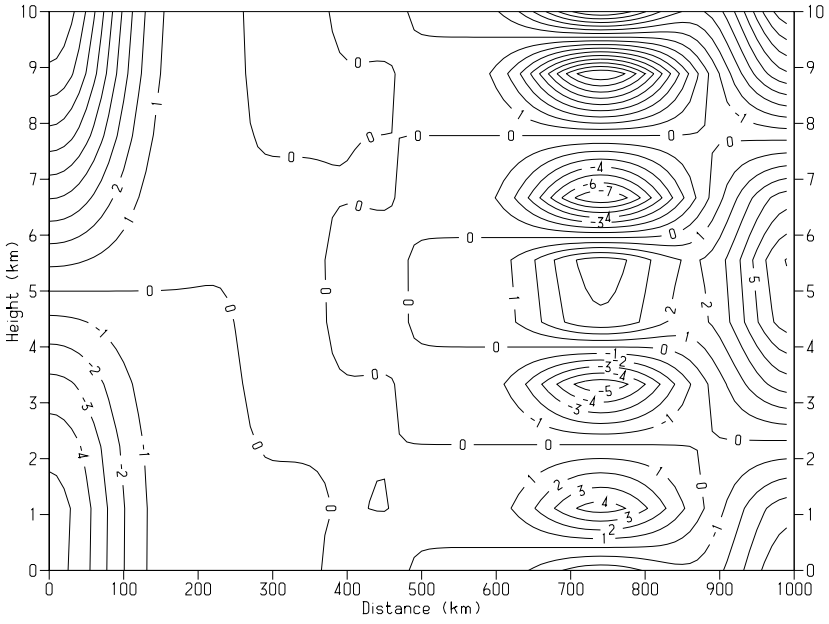

Fig 7. The wind anomaly u' after 108 min.

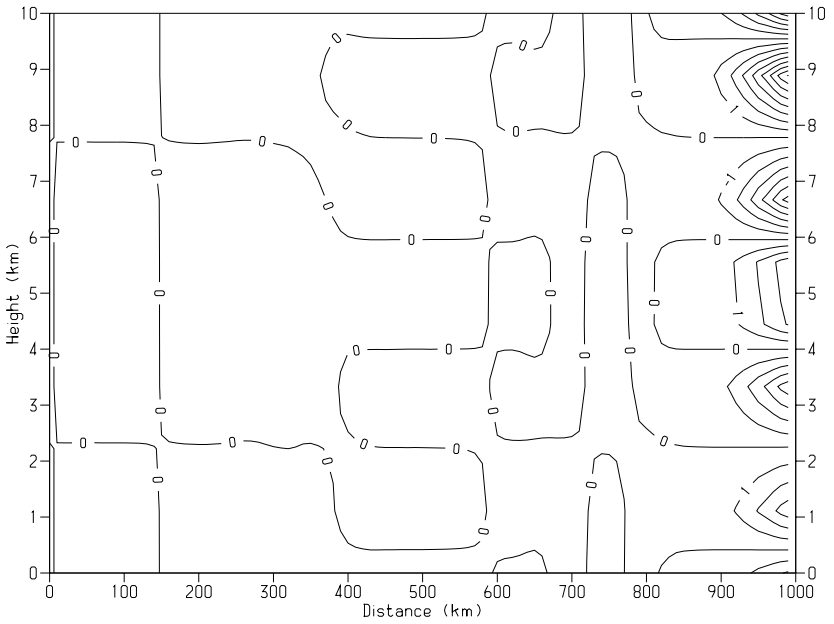

Fig 8. The wind anomaly u' after 237.8 min.

read in at each time-step and used to compute the field W_4 (1/2, $n + 1$) for eq. (A1). All the other W_m associated with incoming waves were put to zero, as described in test 1.

The chart of the u' field after 237.6 min is shown in Fig. 9. In it, the mode 4 field, correctly situated at $x = 360$ km, is easily recognizable from its three nodes. Comparing Fig. 9 with Fig. 8 it is clear that the added complication of the entering wave has not visibly corrupted the integration.

In order to gain more insight into the level of transparency of the boundaries, the rms difference between the W_m and zero

$$\sqrt{\sum_{i=1}^{I} W_m^2(i, n)/I},$$

for each mode $m = 1$, 20, was stored at each time-step. The result is shown in Fig. 10. As can be seen, mode 4 has entered

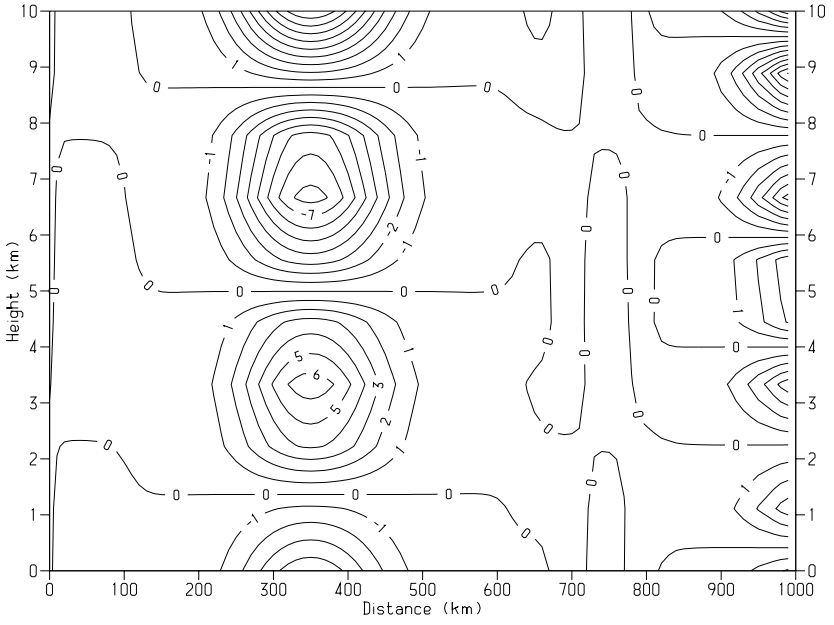

Fig 9. The wind anomaly u' after 237.8 min. now showing that mode 4 has successfully entered the integration area.

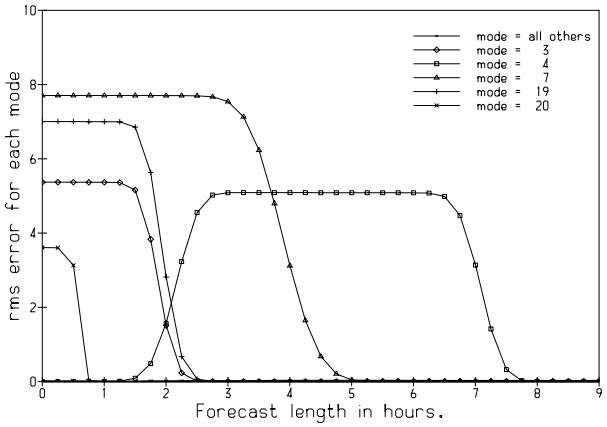

Fig 10. The rms difference between the each of the mode fields W_m, $m = 1, 20$ and zero.

and exited without exciting any visible spurious errors. Also, each of the modes 3, 4, 7, 19 and 20 has exited without exciting visible reflections in any of the potential incoming modes. In fact, at the end of the forecast, after 9 h, the largest reflection is into mode 14 ('mode 7_', so to say); the value is 0.033 modal units. Since the initial value is 7.71 modal units, then by this measure only 0.4% of mode 7 is reflected.

4. Conclusion

Additional urgency has been brought to the question, can the boundary coupling be improved, by the increased use of nested systems in which the innermost area is quite small. If it is small enough for a rapidly moving meteorological feature to cross it during the forecast period, the forecast error in the verification area will be dominated by the errors coming from the inflow boundary after a short time. In such a scenario, if the boundary coupling is inaccurate, the coarser mesh 'host' model forecast will be obviously superior to that of the nested finer mesh 'guest' model. Termonia (2003) gives a nice illustration of the problem. He shows an example in which the host model correctly forecasts severe winds whereas the guest model fails to do so because of boundary errors. In a central forecast office, a model that is inferior in a dramatic forecasting situation, such as a devastating storm, becomes totally discredited even if it is superior in predicting small-scale features in more routine forecasting situations.

This study is part of a programme within the HIRLAM group whose ultimate objective is to find the best possible boundary conditions for a nested non-hydrostatic model. The results presented here are sufficiently encouraging to retain faith in the approach of Engquist and Majda (1977). A concluding quotation from p. 431 of Oliger and Sundström (1978) seems apposite. 'For the hydrostatic equations well-posed problems can only be obtained if the boundary conditions are formulated in terms of local eigenfunction expansions . . . .'

5. Acknowledgments

Thanks to Jim Hamilton for help with the graphics. Thanks to the HIRLAM group for their support and encouragement. The helpful criticism of two anonymous reviewers is also much appreciated.

6. Appendix A: Transforming $\mathbf{W^h}$ to $\mathbf{\Psi}$

This appendix explains how to transform the externally sourced mode fields, $\mathbf{W^h}$, into boundary values for the physical fields, $\mathbf{\Psi}$. For example, consider the situation for the two-layer model when $\bar{u} = 0$. At the western boundary only two boundary fields, W_1 and W_2, are permitted. However, each of these is a linear combination of the four fields, η_1, η_2, u_1 and u_2. The question to be addressed is: how can these externally sourced fields W_1 and W_2 be transformed into boundary values for η_1 and η_2 that knit together seamlessly with u_1 and u_2, which are internal fields on the staggered grid?

In general, let λ_j be tabulated such that $\lambda_1 > \lambda_2 > \cdots > \lambda_K$. (For the two-layer model $K = 4$, but the argument is general.) Suppose $\lambda_j > 0$ for $= 1, l$ and $\lambda_j < 0$ for $j = l + 1, K$.

Thus, at the western boundary the 'l' fields W_j, $j = 1, l$, associated with the incoming waves are imposed. In order to translate the imposition of these mode fields into conditions on the physical fields, first build the fields W such that they are the correct combination of externally imposed fields, designated by the superscript 'h', and internal fields:

$$W_j = \sum_{i=1}^{K} Q^{-1}_{j,i} \Psi^{\mathrm{h}}_i, \quad j = 1, l; \tag{A1}$$

$$W_j = \sum_{i=1}^{K} Q^{-1}_{j,i} \Psi_i, \quad j = l + 1, K. \tag{A2}$$

Here, $\mathbf{\Psi} = (\boldsymbol{\eta}, \mathbf{u})^{\mathrm{t}}$ for the two-layer model and $\mathbf{\Psi} = (\mathbf{p}, \mathbf{u})^{\mathrm{t}}$ for the multilevel model.

At the eastern boundary, where the '$K - l$' fields W_j, $j = l + 1, K$, associated with the incoming waves are imposed, the same procedure is applied with the appropriate alterations to eqs. (A1) and (A2):

$$W_j = \sum_{i=1}^{K} Q^{-1}_{j,i} \Psi^{\mathrm{h}}_i, \quad j = l + 1, K; \tag{A3}$$

$$W_j = \sum_{i=1}^{K} Q^{-1}_{j,i} \Psi_i, \quad j = 1, l. \tag{A4}$$

Now that the correct modes have been designed for the boundaries it only remains to reconstitute the model fields

$$\mathbf{\Psi}^{\mathrm{r}} = \mathbf{QW}, \tag{A5}$$

where the superscript 'r' indicates that the physical fields have been 'reconstituted' as a combination of interior and exterior fields.

There remains the problem of how to handle the staggering of the grid. The least extrapolations are required if $\mathbf{W}$ is constructed at the u points immediately adjacent to the boundaries. Consider the western boundary. To make $\Psi_m(\Delta x/2,\, n+1)$ for $m = 1,\, M$, an interpolation is required for the external host fields and an extrapolation for the internal guest fields. The simplest possible are used in eqs. (A1)–(A4):

$$\Psi_m^{\mathrm{h}}\left(\frac{\Delta x}{2}, n+1\right) = \frac{\Psi_m^{\mathrm{h}}(0, n+1) + \Psi_m^{\mathrm{h}}(\Delta x, n+1)}{2}, \qquad \text{(A6)}$$

$$\Psi_m\left(\frac{\Delta x}{2}, n+1\right) = \frac{3\Psi_m(\Delta x, n+1) - \Psi_m(2\Delta x, n+1)}{2}. \qquad \text{(A7)}$$

On the c-grid no extrapolation is required for $\Psi_i\ (\Delta x/2,\, n+1)$ for $i = M+1,\, K$ since $\mathbf{u}(\Delta x/2,\, n+1)$ has already been updated.

For $m = 1,\, M$ the fields $\Psi_m\ (\Delta x/2,\, n+1)$ reconstituted in eq. (A5) are extrapolated to $x = 0$ via

$$\Psi_m(0, n+1) = 2\Psi_m^r\left(\frac{\Delta x}{2}, n+1\right) - \Psi_m(\Delta x, n+1). \qquad \text{(A8)}$$

This completes the task for the two-layer model. For the multilevel model there is an additional problem, that of deriving the values of $\boldsymbol{\rho}$ and $p_{1/2}$. To see how to do this, multiply eq. (3.27) by $\boldsymbol{\tau}^{-1}$, multiply eq. (3.34) by $\mathbf{E}\boldsymbol{C}^{-2}$ and subtract

$$\frac{\mathrm{d}}{\mathrm{d}t}(\boldsymbol{\tau}^{-1}\boldsymbol{\rho} - \mathbf{E}\boldsymbol{C}^{-2}\mathbf{E}^{-1}\mathbf{p}) = 0, \qquad \text{(A9)}$$

a solution of which is

$$\boldsymbol{\rho} = \boldsymbol{\tau}\mathbf{E}\mathbf{C}^{-2}\mathbf{E}^{-1}\mathbf{p}. \qquad \text{(A10)}$$

Also, multiply eq. (3.34) by $\mathbf{E}\,\boldsymbol{C}^{-2}$ and substitute the resulting value of $\partial\mathbf{u}/\partial x$ in eq. (3.28). This yields an equation which has as a solution

$$p_{1/2} = \boldsymbol{\nu}\mathbf{E}\mathbf{C}^{-2}\mathbf{E}^{-1}\mathbf{p}. \qquad \text{(A11)}$$

It is easy to show that these are compatible with eq. (3.29).

In the integrations described in Section 3.2 $\boldsymbol{\rho}^r(\Delta x/2,\, n+1)$ and $p_{1/2}^r(\Delta x/2,\, n+1)$ were generated via eqs. (A10) and (A11) and subsequently extrapolated to $x = 0$ using the same extrapolation as in eq. (A8).

The extrapolations at the eastern boundary are performed in the same way.

References

Davies, H. C. 1976. A lateral boundary formulation for multi-level prediction models. *Q. J. R. Meteorol. Soc.* **102**, 405–418.

Davies, H. C. 1983. Limitations on some common lateral boundary schemes used in regional NWP models. *Mon. Wea. Rev.* **111**, 1002–1012.

Doetsch, G. 1971. In: *Guide to the Application of the Laplace and Z-Transforms*, Van Nostrand-Reinhold, Princeton, NJ, 240 pp.

Durran, D. R. 2001. Open boundary conditions: fact and fiction. In: *IUTAM Symposium on Advances in Mathematical Modelling of Atmosphere and Ocean Dynamics*, (ed.P. F. Hodnett), Kluwer Academic, Dordrecht, 1–18.

Durran, D. R., Yang, M. J. and Brown, R. G. 1993. Toward more accurate wave-permeable boundary conditions. *Mon. Wea. Rev.* **121**, 604–620.

Engquist, B. and Majda, A. 1977. Absorbing boundary conditions for the numerical simulation of waves. *Math. Comput.*, **31**, 629–651.

Gill, A. E. 1982. In: *Atmosphere–Ocean Dynamics*. Academic Press, New York, 662 pp.

Gustafsson, B., Kreiss, H.-O. and Oliger, J. 1995. In: *Time-Dependent Problems and Difference Methods*. Wiley, New York, 642 pp.

Ince, E. L. 1956. In: *Ordinary Differential Equations*. Dover, New York, 558 pp.

Kalnay, E. 2003. In: *Atmospheric Modeling, Data Assimilation, and Predictability*. Cambridge Univ. Press, Cambridge, 341 pp.

McDonald, A. 2000. Boundary conditions for semi-Lagrangian schemes; testing some alternatives in one-dimensional models. *Mon. Wea. Rev.* **128**, 4084–4096.

McDonald, A. 2002. A step toward transparent boundary conditions for meteorological models. *Mon. Wea. Rev.* **130**, 140–151.

Marbaix, P., Galleée, H., Brasseur, O. and van Ypersele, J.-P. 2003. Lateral boundary conditions in regional climate models: a detailed study of the relaxation procedure. *Mon. Wea. Rev.* **131**, 462–479.

Met.O.1012, 1993. In: *Forecasters' Reference Book*. Meteorological Office, 191 pp.

Oliger, J. and Sundström, A. 1978. Theoretical and practical aspects of some initial boundary value problems in fluid dynamics. *J. Appl. Math.* **35**, 419–446.

Robert, A. 1966. The integration of a low order spectral form of the primitive meteorological equations. *J. Meteorol. Soc. Japan* **44**, 237–245.

Termonia, P. 2003. Monitoring and improving the the temporal interpolation of lateral boundary coupling data for limited area models. *Mon. Wea. Rev.* **131**, 2450–2463.

Tsynkov, S. V. 1998. Numerical solutions of problems on unbounded domains. A review. *Appl. Numer. Math.* **27**, 465–532.